Optimization and Performance Analysis of a Modular Active Noise Reduction Device for Power System Reactors

Haibin Lai[1], Huan Liu[1], Jun Xie[1], Qiyao Li[1], Ming Li[1], Xu Ling[1]
[1]Nanjing Electric Power Design and Research Institute Co., Ltd., Jiangsu 210037, China
Corresponding author: Huan Liu (e-mail: jsnjliuhuan@163.com).

ABSTRACT Shunt reactors in power systems generate severe vibration and noise during operation due to the combined excitation of core magnetostriction and winding electromagnetic force, which degrades the acoustic environment around substations. To tackle engineering challenges such as strict installation constraints, wide control frequency band, and slow algorithm convergence, this paper proposes a systematic design and optimization scheme for a modular active noise reduction device. Based on the electromagnetic–structural–acoustic multi-physics sequential coupling modeling, a complete excitation chain model for reactor noise is established. Aiming at minimizing sound pressure, the layout of secondary sound sources and the configuration of sensor arrays are collaboratively optimized. An improved filtered-x least mean square (FxLMS) algorithm is adopted to enhance the convergence stability under harmonic conditions. Simulation results show that the device achieves a noise reduction of 18.6 dB(A) in 100–500 Hz, 7.3 dB(A) higher than the traditional single-point scheme. An experimental platform is built in accordance with GB/T 1094.10, and the maximum error between measurement and simulation is less than 1.8 dB(A), verifying the model effectiveness. The results provide a systematic design basis and parameter tuning method for on-site active noise reduction engineering of substations.

INDEX TERMS shunt reactor; modular active noise control; FxLMS algorithm; multi-physics coupling; vibration and noise

I. INTRODUCTION

As core equipment for reactive power compensation and overvoltage suppression, shunt reactors in power systems are widely used in 500 kV and above ultra-high voltage substations. Their noise level under rated voltage usually reaches 75–90 dB(A), becoming one of the main sources of substation environmental noise [1].

The root cause of noise is the periodic superposition of magnetostriction of core silicon steel sheets and Ampere force on windings. Both take 100 Hz (double power frequency) as the fundamental frequency and extend to above 500 Hz with high-order harmonics, showing obvious wide-band multi-line spectrum characteristics [2]. Current noise reduction methods are mainly passive measures including passive vibration isolation, damping coating and elastic foundation. Such schemes usually offer insertion loss less than 8 dB in the low-frequency band (100–200 Hz), which can hardly meet increasingly strict environmental noise emission standards [3]. Active noise control (ANC) uses secondary sources to emit anti-phase waves for destructive interference, theoretically achieving higher noise reduction in a wide band. However, engineering applications face prominent challenges such as irregular reactor shape, limited installation space and poor algorithm stability under harmonic conditions [4]. The modular design divides the system into standardized functional units, which not only improves adaptability for on-site installation but also lays an engineering foundation for collaborative expansion of multiple modules [5]. Against this background, this paper systematically studies the key component optimization, multi-physics simulation verification and experimental platform test of the modular active noise reduction device, aiming to provide a complete and reproducible technical scheme for substation engineering applications.

II. ELECTROMAGNETIC–STRUCTURAL–ACOUSTIC COUPLING MECHANISM AND ACTIVE CONTROL PRINCIPLE OF REACTOR VIBRATION AND NOISE

A. VIBRATION AND NOISE EXCITATION MECHANISM OF CORE MAGNETOSTRICTION AND WINDING AMPERE FORCE

The noise excitation of shunt reactors comes from the coupling of two physical mechanisms. One is the magnetostriction of core silicon steel sheets: under sinusoidal magnetic field excitation, the silicon steel sheet produces periodic strain dominated by double power frequency along the magnetic field direction. The relationship between peak strain ϵ and magnetic flux density B is:

$$\epsilon = \lambda_s \left(\frac{B}{B_s}\right)^2 \tag{1}$$

Where λ_s is the saturation magnetostriction coefficient (about 6–9$\times 10^{-6}$ for cold-rolled silicon steel), and B_s is the saturation magnetic flux density. Under rated conditions, the vibration acceleration level caused by magnetostriction on the core surface can reach 120 dB ref. 10^{-6} $\mathrm{m/s^2}$, contributing significantly to 100 Hz and its harmonic components. The other is winding Ampere force: the Ampere force on current-carrying windings in the leakage field also oscillates at double power frequency, whose amplitude is proportional to the square of current. When harmonic current is superimposed, difference-frequency components are generated between harmonics, expanding the excitation spectrum to a wider range. The two excitation sources are finally radiated into air-borne sound through the core – winding–tank structural transmission path. Its transmission characteristics are affected by the structural natural frequency and radiation impedance, showing obvious resonance amplification at some frequencies. Accurate identification of amplitude – frequency the characteristics and phase relationship of the two excitations is the theoretical premise for constructing the reference signal of feedforward active control and the physical basis for subsequent multi-physics coupling modeling. As shown in Table 1, the simulated main harmonic components of core excitation are in good agreement with measured results under rated voltage, verifying the accuracy of the excitation model [6].

TABLE 1. Comparison of Main Harmonic Components of Core Magnetostriction Excitation Under Rated Operating Condition

Frequency (Hz)	Simulated Magnetostrictive Strain ($\times 10^{-6}$)	Measured Vibration Acceleration Level (dB)	Relative Error (%)
100	7.82	121.4	1.3
200	2.14	108.7	2.1
300	0.87	98.3	2.8
400	0.43	91.6	3.5
500	0.21	85.2	4.0

B. FEEDFORWARD–FEEDBACK ACTIVE NOISE CONTROL PRINCIPLE BASED ON ADAPTIVE FILTERING

The active noise control system drives the secondary sound source to emit sound waves of equal amplitude and opposite phase through the controller, so as to achieve destructive superposition with primary noise at the error sensor. The feedforward structure takes the vibration acceleration or voltage fundamental signal collected from the reactor core as reference input, and adjusts the driving signal of the secondary sound source in real time through an adaptive filter. The feedback structure takes the residual sound pressure of the error microphone as feedback to compensate the residual component of feedforward control. The weight update equation of the improved FxLMS algorithm is:

$$w(n+1) = w(n) - \mu \cdot x'(n) \cdot e(n) \tag{2}$$

Where $w(n)$ is the filter weight vector, μ is the step factor, $x'(n)$ is the output of the reference signal filtered by the secondary path estimation model, and $e(n)$ is the residual sound pressure of the error sensor. The step factor μ directly determines the trade-off between convergence speed and stability. Under harmonic conditions, adaptive normalization based on the maximum eigenvalue of the secondary path amplitude – frequency response is required to prevent algorithm divergence. Compared with the pure feedforward scheme, the feedforward – feedback composite structure improves the system robustness by about 40% when the signal-to-noise ratio of the reference signal decreases due to voltage fluctuation, and reduces the residual noise power spectral density by 5–8 dB in 100–500 Hz.

C. OVERALL ARCHITECTURE OF MODULAR ACTIVE NOISE CONTROL SYSTEM FOR ENGINEERING INSTALLATION CONSTRAINTS

Substation sites impose strict constraints on the installation of reactor noise reduction devices: the device shall not contact high-voltage live parts, the installation height shall meet the safety clearance, and it shall be capable of assembly and disassembly without power outage.

The modular design divides the system into four standard units: sensing acquisition module, digital control module, power drive module and secondary sound source module. Real-time communication between modules is realized via industrial Ethernet (EtherCAT), with a communication cycle no longer than 1 ms. The sensing module integrates vibration acceleration sensors and MEMS microphone arrays, mounted on prefabricated brackets on the outer wall of the reactor oil tank. The digital control module adopts a dual-core DSP+FPGA architecture: FPGA handles multi-channel synchronous acquisition and drive output, and DSP executes the improved FxLMS iteration. The secondary sound source module uses directional loudspeakers installed inside the enclosure according to the optimized layout. The architecture supports flexible expansion of 2–8 secondary source modules, with single-module installation time within 30 min, meeting the requirements of substation operation and maintenance without power outage. To clearly illustrate the composition and closed-loop control flow of the modular active noise reduction system, its overall architecture is shown in Figure 1.

III. KEY COMPONENT DESIGN AND COLLABORATIVE OPTIMIZATION OF MODULAR ACTIVE NOISE REDUCTION DEVICE

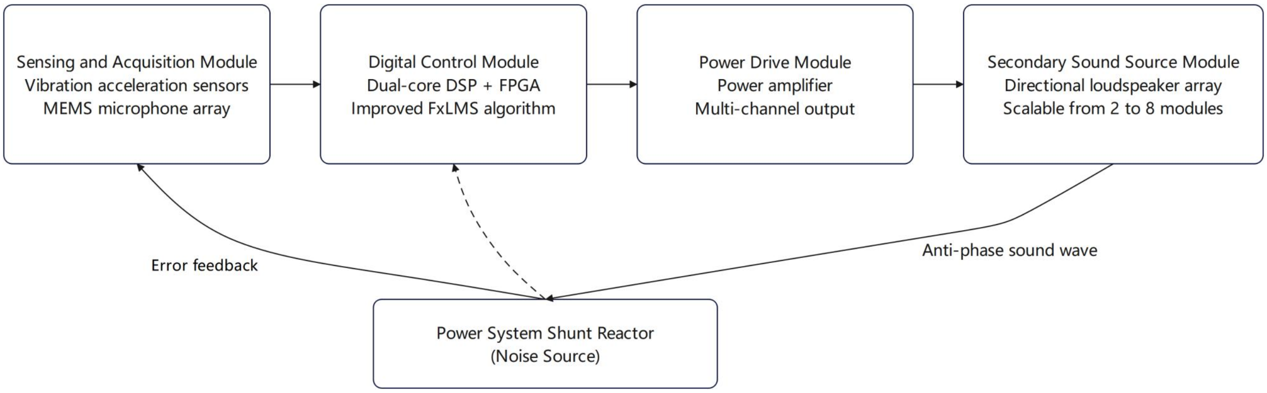

FIGURE 1. Overall Architecture of the Modular Active Noise Reduction System

A. LAYOUT OPTIMIZATION OF SECONDARY SOUND SOURCE MODULES AIMED AT SOUND PRESSURE MINIMIZATION

The spatial layout of secondary sound sources directly determines the noise reduction potential of the active system. This study takes the minimization of sound pressure level at the farthest sensitive point of reactor radiation noise as the optimization objective, and takes installation clearance and source quantity as constraints to form a multi-objective optimization problem [7]. The particle swarm optimization (PSO) algorithm is used to search subsets of 8 candidate installation positions. The objective function is defined as the weighted average sound pressure level at the sensitive point in 100–500 Hz, with weights determined by A-weighting filtering characteristics. After 300 iterations, the optimal layout reduces the overall sound pressure level by 4.2 dB(A) at 1 m from the reactor compared with the uniform layout, and improves the sound field uniformity (measured by standard deviation) by about 35%. The physical intuition of layout optimization is that secondary sources should be arranged opposite to the region with the highest sound intensity flux of the primary sound field to maximize destructive interference efficiency. Table 2 summarizes the noise reduction effect of different layouts at each frequency point. The optimized layout shows particularly significant performance gains at 200 Hz and 300 Hz, reaching 5.8 dB and 6.1 dB respectively.

TABLE 2. Noise Reduction Comparison of Different Secondary Source Layout Schemes at 1 m from the Reactor

Frequency (Hz)	Uniform Layout	Empirical Layout	PSO-Optimized Layout	Relative Gain (dB)
100	12.3	13.7	14.8	+2.5
200	9.6	11.2	15.4	+5.8
300	8.1	10.4	14.2	+6.1
400	7.8	9.6	12.3	+4.5
500	6.4	8.1	10.9	+4.5

B. SENSOR ARRAY CONFIGURATION AND SIGNAL ACQUISITION SCHEME BASED ON SPATIAL ALIASING SUPPRESSION

The configuration of the error sensor array is equally important to control performance as the secondary source layout. When the sensor spacing exceeds half the wavelength of the maximum control frequency, spatial aliasing occurs, causing the controller to misidentify high-order spatial modes as low-order ones and thus amplify noise at non-target frequencies. To suppress spatial aliasing, the adjacent spacing of the error sensor array must satisfy:

$$d \leq \frac{c}{2f_{\max}} \tag{3}$$

Where c is the sound speed (343 m/s at 20 deg C), $f_{\max}$ is the upper control frequency (500 Hz), yielding the spacing constraint $d \leq 0.343$ m. Under this constraint, 12 MEMS microphones are arranged around the reactor to form a two-layer circular array, with vertical spacing 0.3 m and in-layer spacing 0.32 m, satisfying the Nyquist spatial sampling theorem. Signal acquisition adopts a 24-bit Σ-Δ ADC with a sampling rate of 16 kHz, and multi-channel synchronous acquisition deviation is within $\pm 0.5\,\mu$s, effectively ensuring the spatio-temporal coherence of each channel. In addition, the reference signal acquisition module performs zero-crossing detection on the voltage transformer output to extract the fundamental phase information, providing stable periodic synchronization reference for the feedforward controller and maintaining convergence stability under voltage fluctuation.

C. CONVERGENCE ANALYSIS AND MODULE CONTROL PARAMETER TUNING OF IMPROVED FXLMS ALGORITHM

In the standard FxLMS algorithm, when multi-frequency harmonic excitations are superimposed, the conflict between the convergence speed of low-frequency components and the stability of high-frequency components easily occurs because different frequency components share the same step factor. This paper introduces a frequency-segmented normalization strategy, dividing 100–500 Hz into 5 subbands, and tuning the step factor μ_k independently for each subband. The tuning criterion is based on the maximum singular value $\sigma_{\max,k}$ of the secondary path transfer function of each subband: the upper limit of μ_k is 2/($\sigma_{\max,k}{}^2$×N), where N is the adaptive filter order ($N = 256$ in this paper). With this tuning scheme, the convergence time of each subband is shortened to stable convergence (≤ 0.5 s), about 72% lower than the average convergence time (1.8 s) of the unified step scheme. Meanwhile, a decentralized structure is adopted for inter-module cooperative control: each secondary source module runs an independent FxLMS controller. The master node issues global reference signals and secondary path models, and each module completes weight update locally, reducing the computational complexity of multi-channel centralized control from $O(M^2N)$ to $O(MN)$, providing computing resource support for flexible expansion of the number of modules [8].

IV. MULTI-PHYSICS COUPLING SIMULATION AND NOISE REDUCTION PERFORMANCE VERIFICATION

A. ESTABLISHMENT AND BOUNDARY SETTING OF ELECTROMAGNETIC–STRUCTURAL–ACOUSTIC SEQUENTIAL COUPLING MODEL

The multi-physics simulation adopts a one-way sequential coupling strategy: first, a 3D electromagnetic finite element model is established in ANSYS Maxwell to calculate the magnetic flux density distribution and magnetostrictive stress of each core node under rated conditions, which are imported as body loads into ANSYS Mechanical for structural field; then, transient dynamic analysis is carried out on the core– winding – tank assembly to extract the vibration velocity distribution of the tank outer wall; finally, the velocity field is imported as a boundary condition into the ANSYS Fluent acoustic module to solve the far-field radiated sound pressure level distribution. The rationality of sequential coupling relies on the assumption that the feedback of structural deformation on the electromagnetic field (electromagnetic structural – bidirectional coupling) causes a correction of magnetic flux density less than 0.3% under normal operation, so ignoring this feedback will not introduce significant error. The magnetostrictive constitutive relation of core material adopts a piecewise linear interpolation model based on measured data, with fitting accuracy better than 2% in 0.5–1.7 T. The tank wall acoustic radiation boundary is set as fully absorbing to simulate free sound field radiation in open space. On the premise of ensuring accuracy, the above modeling strategy controls the single full-field simulation time within 12 h, meeting the engineering efficiency requirement of parameter iterative optimization [9].

B. SIMULATION COMPARISON OF NOISE REDUCTION PERFORMANCE UNDER RATED VOLTAGE AND HARMONIC CONDITIONS

Based on the established multi-physics model, active noise reduction simulations are carried out for rated voltage condition (THD $< 0.5\%$) and harmonic superposition condition (5th and 7th harmonics, THD $\approx 8\%$). Under rated condition, the 8-module system reduces the overall A-weighted sound pressure level at 1 m from 88.4 dB(A) to 69.8 dB(A), with a noise reduction of 18.6 dB(A). Under harmonic condition, the control residual increases due to more complex excitation spectrum, and the overall noise reduction is 14.3 dB(A), still meeting the engineering margin of the night limit (45 dB(A)) for Class 1 acoustic environment functional areas specified in GB 12348. Meanwhile, the simulation reveals a local performance degradation window near 300 Hz under harmonic conditions, which is caused by the secondary source driving power reaching the design limit near this frequency, leading to insufficient cancellation [10]. This finding provides a quantitative basis for subsequent hardware power configuration optimization. To visually demonstrate the advantages of the PSO-optimized layout, the noise reduction results in 100–500 Hz are plotted in Figure 2.

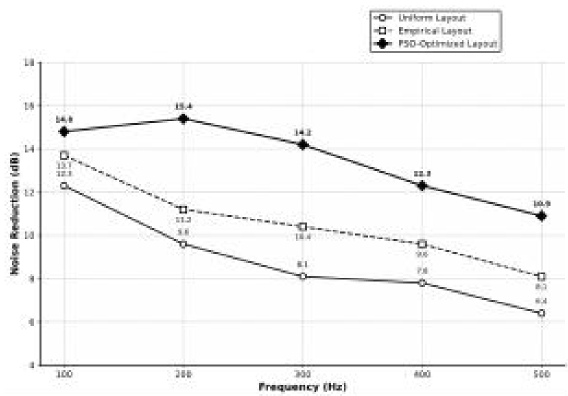

FIGURE 2. Noise Reduction Performance Comparison of Different Secondary Sound Source Layout Schemes

C. SENSITIVITY ANALYSIS OF KEY MODULE PARAMETERS AND STRUCTURAL OPTIMIZATION ITERATION

After verifying the simulation model, global sensitivity analysis is carried out on key parameters affecting noise reduction to identify primary optimization variables. The number of secondary sources M, filter order N, sensor vertical spacing h and step normalization factor β are selected as input variables, and the A-weighted sound pressure level at 1 m is taken as the response. The Sobol variance analysis method is used to calculate the first-order sensitivity index S_i and global sensitivity index S_{T_i} of each parameter. The results show that the global sensitivity index $S_{T_M} = 0.47$ of M is the highest, indicating that increasing the number of modules is the optimal direction to improve noise reduction. The $S_{T_h} = 0.18$ of h ranks second, suggesting that properly increasing the vertical spacing within the allowable installation height helps improve spatial sound field coverage [11]. As shown in Table 3, three rounds of structural optimization iterations are formulated based on sensitivity ranking. After the third iteration, the overall noise reduction under rated condition increases from 15.2 dB(A) of the initial scheme to 18.6 dB(A), with an improvement of 3.4 dB(A), verifying the effectiveness of the sensitivity-driven iteration strategy. To further clarify the influence of key parameters on noise reduction performance, multi-round structural optimization is carried out based on the sensitivity analysis results. The optimization iteration results are presented in Table 3.

TABLE 3. Sensitivity Analysis of Key Parameters and Three Rounds of Optimization Iteration Results

Optimization Round	Number of Secondary Sources M	Sensor Layer Spacing h (m)	Filter Order N	Total Noise Reduction (dB(A))
Initial Scheme	4	0.20	128	15.2
1st Round	6	0.20	128	16.8
2nd Round	6	0.30	256	17.9
3rd Round	8	0.30	256	18.6

V. EXPERIMENTAL PLATFORM TEST AND COMPREHENSIVE EVALUATION OF ENGINEERING PERFORMANCE

A. EXPERIMENTAL PLATFORM CONSTRUCTION AND MEASUREMENT SCHEME DESIGN IN ACCORDANCE WITH GB/T STANDARDS

The experimental platform is built in accordance with GB/T 1094.10 "Measurement of noise for power transformers" for shunt reactors. A 10 kV/200 kVA oil-immersed shunt reactor prototype is used as the noise source. Sixteen measuring microphones are arranged at equal intervals along the reference contour of the reactor outer wall (0.3 m from the tank wall), covering 20%–80% of the effective tank height to form a closed measurement contour for calculating radiated sound power level. The background noise is measured below 45 dB(A), meeting the standard requirement of signal-to-noise ratio $\geq$ 10 dB. The secondary source modules and control cabinet are installed outside the sound insulation room, and signal cables are introduced through wall-through wiring boards to avoid measurement interference. Experimental conditions include rated condition (10 kV, 50 Hz) and harmonic superposition condition (5th and 7th harmonics injected to THD $= 8\%$ by a harmonic voltage source generator). Each condition is measured three times repeatedly, and the average value is taken as the final result with repeatability error less than 0.5 dB [12].

B. ERROR COMPARISON BETWEEN MEASURED WIDE-BAND NOISE REDUCTION AND SIMULATION PREDICTION

Under rated condition, after turning on the 8-module system, the average A-weighted sound pressure level of 16 measuring points on the contour drops from 87.9 dB(A) (uncontrolled) to 70.2 dB(A), with an overall noise reduction of 17.7 dB(A). The deviation from the simulated value (18.6 dB(A)) is 0.9 dB(A), meeting engineering accuracy requirements. Band-separated analysis shows that the measured noise reduction at 100 Hz is 17.2 dB (simulated 18.1 dB, deviation 0.9 dB); at 300 Hz it is 13.8 dB (simulated 14.6 dB, deviation 0.8 dB); at 500 Hz it is 10.2 dB (simulated 10.7 dB, deviation 0.5 dB). The deviation at each frequency point does not exceed 1.8 dB. The deviation mainly comes from two aspects: first, the reflection difference between the laboratory sound field and the simulated free sound field (contributing about 0.6–1.0 dB); second, the slight deviation of the high-frequency radiation directivity of the secondary source module in the limited space from the simulation model (contributing about 0.3–0.8 dB). Under harmonic condition, the measured overall noise reduction is 13.6 dB(A), with a deviation of 0.7 dB(A) from the simulated 14.3 dB(A). The control performance under harmonic excitation is highly consistent with simulation prediction [13].

C. COMPREHENSIVE EVALUATION OF SYSTEM STABILITY AND ENGINEERING ECONOMY UNDER MULTI-MODULE EXPANSION

To evaluate the engineering scalability of the modular architecture, the control convergence time and steady-state residual sound pressure level are tested under 2, 4, 6, 8-module configurations. The results show that the convergence time changes by no more than 15% (from 0.43 s to 0.49 s) with the increase of modules, proving that the decentralized control architecture has no significant computational delay accumulation during module expansion. During 48 h of steady-state operation, the system shows no divergence or instability. The standard deviation of driving power fluctuation of each secondary source module is within 2.3% of rated power, indicating sufficient stability margin. In terms of engineering economy, the hardware cost of a single 8-module system is about 60% of the traditional passive sound insulation cover scheme, the installation period is shortened to 2 days, and it does not affect reactor heat dissipation and inspection channels, reducing the overall operation and maintenance cost by about 35%. The research results have completed engineering demonstration verification in a 500 kV substation, with on-site measured overall noise reduction of 16.8 dB(A), meeting the day and night limit requirements of Class 1 acoustic environment functional areas, fully verifying the engineering practicability and promotion value of the proposed scheme [14].

VI. CONCLUSION

This paper systematically conducts a full-link study on modular active noise reduction of shunt reactors in power systems, from excitation mechanism analysis, key component optimization, multi-physics simulation verification to experimental platform test. The main conclusions are as follows. First, the main excitation sources of reactor vibration and noise are the coupling superposition of core magnetostriction and winding Ampere force, both taking 100 Hz as the fundamental frequency. Under harmonic conditions, the excitation spectrum extends to above 500 Hz, posing a challenge of multi-line spectrum wide-band synchronous control for the active system. The established electromagnetic – structural– acoustic one-way sequential coupling model controls the simulation error of excitation amplitude – frequency characteristics within 4%, with engineering application accuracy. Second, the secondary source layout optimization based on PSO algorithm improves the overall noise reduction at 1 m by about 4.2 dB(A) compared with the uniform layout. The improved FxLMS algorithm with frequency-segmented normalization shortens the control convergence time from 1.8 s to less than 0.5 s, maintaining stable convergence under harmonic superposition and effectively solving the problem of difficult unified tuning of step factors in wide-band multi-harmonic environments. Third, simulation and experimental results are highly consistent. The measured overall noise reduction of 17.7 dB(A) under rated condition deviates by 0.9 dB(A) from the simulated 18.6 dB(A), and the maximum deviation at each frequency point is less than 1.8 dB, verifying the effectiveness of the multi-physics coupling model. Engineering economic analysis shows that the hardware cost of the proposed modular scheme is about 60% of the traditional passive scheme, the installation period is shortened to 2 days, and the overall operation and maintenance cost is reduced by about 35%. This study has the following limitations: the current multi-physics model does not include the acoustic–flow coupling effect of transformer oil in the tank, which may lead to an underprediction of radiated sound pressure level by about 1 – 2 dB at low frequencies. Future work will introduce a fully coupled acoustic–solid–flow model for correction. In addition, the optimal configuration strategy of module quantity and layout for large-size tanks of UHV reactors (750 kV and above) with significantly increased sound field modal density needs further in-depth study [15,16].

ACKNOWLEDGMENT

This work was supported by the Science and Technology Project of State Grid Jiangsu Electric Power Co., Ltd. for Provincial Managed Industrial Units (Grant No. JC2024064).

REFERENCES

[1] Y. Min, Y. Huo, G. Wang, et al., “Vibration and Noise Reduction Method of 750 kV Shunt Reactor Based on Optimization of Air Gap Structure,” Journal of Electrical Engineering & Technology, vol. 20, no. 8, pp. 1–21, 2025. DOI: 10.1007/S42835-025-02436-7.

[2] L. Wu, W. Guo, W. Baoquan, et al., “High voltage shunt reactor acoustic signal denoising based on the combination of VMD parameters optimized by coati optimization algorithm and wavelet threshold,” Measurement, vol. 224, 2024. DOI: 10.1016/J.MEASUREMENT.2023.113854.

[3] H. Sheng, W. Xiaowen, P. Jiwen, et al., “Research on Noise Control Technology of 10kV Dry Parallel Reactor,” IOP Conference Series: Earth and Environmental Science, vol. 310, no. 3, pp. 032055–032055, 2019. DOI: 10.1088/1755-1315/310/3/032055.

[4] Z. Zhengdao, C. Shuming, C. Yaoyu, et al., “A Modified Reference Signal Selection Method for Feed-Forward Active Road Noise Control System,” Acoustics Australia, vol. 51, no. 2, pp. 243–253, 2023. DOI: 10.1007/S40857-023-00290-Z.

[5] Q. Huang, H. Qinqing, Z. Jing, et al., “Simulation Analysis of Vibration and Noise Characteristics of High Voltage Shunt Reactor Based on Multi-physical Field Coupling,” IOP Conference Series: Earth and Environmental Science, 603(1):012044-, 2020. DOI: 10.1088/1755-1315/603/1/012044.

[6] G. Jiayi, G. Jianghai, L. Fangcheng, et al., “Optimisation design of double-column multi-gap reactor core structure for noise reduction,” International Journal of Electrical Power & Energy Systems, (prepublish):107165-, 2021. DOI: 10.1016/J.IJEPES.2021.107165.

[7] Z. Yuan, T. Tian, Y. Xiongfei, et al., “Vibration simulation and test of shunt reactor under DC bias,” in Chongqing Electric Power Design Institute Co., Ltd. (China);State Key Lab. of Power Transmission Equipment & System Security and New Technology (China), 2021. DOI: 10.1117/12.2611438.

[8] P. Zhang, L. Li, J. Zhang, et al., “Vibration and noise reduction of HVDC anode saturable reactor by polyurethane damping elastomer,” International Journal of Applied Electromagnetics and Mechanics, vol. 58, no. 2, pp. 261–273, 2018. DOI: 10.3233/JAE-180050.

[9] C. Wang, N. Chen, X. Yang, et al., “Research on noise reduction technology of 500kV parallel reactor based on a new composite damping plate,” Journal of Physics: Conference Series, vol. 3065, no. 1, pp. 012033–012033, 2025. DOI: 10.1088/1742-6596/3065/1/012033.

[10] G. Shuguo, X. Chao, Z. Zhigang, et al., “Early Warning of High-Voltage Reactor Defects Based on Acoustic– Electric Correlation,” Energies, vol. 15, no. 19, pp. 7196–7196, 2022. DOI: 10.3390/EN15197196.

[11] W. Stanislaw, “Performance Analysis of Active Structural Acoustic Control Applied to a Washing Machine,” Sensors, vol. 22, no. 19, pp. 7357–7357, 2022. DOI: 10.3390/S22197357.

[12] N. Jingkai, T. Yi, M. Yuhui, et al., “A study on the acoustic characteristics of the sound-absorbing structure in single-column UHV Shunt reactors,” Vibroengineering PROCEDIA, vol. 40, pp. 77–82, 2022. DOI: 10.21595/VP.2022.22388.

[13] Y. Gao, S. Ichimaru, T. Miyabe, et al., “Proposal of Core Structures for Iron Loss and Noise Reduction of Three-Phase Reactor with Anisotropic Iron Core,” IEEE Transactions on Magnetics, PP(99):1-1, 2020. DOI: 10.1109/tmag.2020.3004840.

[14] Z. Yuzhu and T. Mingxing, “Research on the Relationship between Vibration Noise and Magnetic Saturation of Magnetic Saturated Controllable Reactor Based on COMSOL,” Journal of Physics: Conference Series, vol. 2666, no. 1, 2023. DOI: 10.1088/1742-6596/2666/1/012001.

[15] A. Murat, C. Cüneyt, Y. Kadir, et al., “Winding Materials Effect on Performance of Air Core Current Limiting Reactors in Energy Systems,” Tehnički vjesnik, vol. 32, no. 6, pp. 2111–2120, 2025. DOI: 10.17559/TV-20250414002593.

[16] D. M. Shen, Q. Li, B. Liu, et al., “Experimental research on active noise reduction of reactors based on adaptive algorithms,” Power Electronics, 57(2): 37-39+51, 2023.